Article

Enhanced Photodegradation of Sulfamethoxazole Through Cutting-Edge Titania-Zirconia-Based Materials

Zineb Bensmaine [1], Sanaa El Korso [1], Adriana Isabel Moral-Rodríguez [2], Sumeya Bedrane [1], Chewki Ziani-Cherif [1], Agustín Francisco Pérez-Cadenas [2], Francisco Carrasco-Marín [2] and Esther Bailón-García [2,*]

[1] Laboratory of Catalysis and Synthesis in Organic Chemistry, Chemistry Department, Science Faculty, University of Tlemcen, Tlemcen B.P. 119, Algeria; zineb.bensmaine94@gmail.com (Z.B.); sanaa.hamzareguig@univ-tlemcen.dz (S.E.K.); sumeya.bedrane@univ-tlemcen.dz (S.B.); czcherif@yahoo.fr (C.Z.-C.)

[2] Materiales Polifuncionales Basados en Carbono (UGR-Carbon), Facultad de Ciencias, Universidad de Granada, Campus Fuente Nueva s/n, 18071 Granada, Spain; ady_moral@hotmail.com (A.I.M.-R.); afperez@ugr.es (A.F.P.-C.); fmarin@ugr.es (F.C.-M.)

* Correspondence: estherbg@ugr.es

Abstract: ZrO_2, TiO_2, ZrO_2-TiO_2, and TiO_2-ZrO_2 were successfully prepared using the sol–gel method and fully characterized to check their physico-chemical features. X-ray diffraction showed the co-existence of monoclinic and tetragonal ZrO_2 in addition to the Anatase phase for TiO_2. The formation of mixed oxides led to a reduction in the band gap values and a modification of the textural characteristics, while the XPS evidenced an oxygen vacancy-rich surface. The ability of the synthesized materials to eliminate drug contaminants was checked using Sulfamethoxazole (SMX) as a model molecule under UV and BLUE-LED irradiation. The materials' potential to decrease wastewater toxicity was also studied. The best photocatalyst was TiO_2-ZrO_2 with 76 and 100% conversion under visible and UV irradiation, respectively.

1. Introduction

Water pollution is one of the most dangerous environmental problems in the world; it poses many risks to human life and the environment. Increasing human and industrial activities also increase the amount of wastewater rejected into water resources. Organic dyes are considered dangerous pollutants due to their low rate of biodegradability and high toxicity. Therefore, they are considered one of the most pernicious wastewaters [1]. Pharmaceutical compounds, also considered emerging environmental contaminants due to their endocrine perturbation properties, are either naturally occurring or synthetically produced [2]. Today, approximately 3000 different compounds are used as drugs in human and veterinary healthcare [3]. They belong to a wide range of different chemical structures. In addition to the well-known compounds, the large number of excreted metabolites (secondary products) must be taken into account. Antibiotics belong to important compounds; they are widely utilized in both human and veterinary medicine and in aquaculture for the prevention or treatment of microbial infections. Additionally, they are used in livestock production to enhance animal growth [4]. The enduring and harmful characteristics of these compounds pose a significant challenge to their complete removal via standard wastewater treatment methods. Consequently, there is an urgent need for innovative technologies that can effectively treat these compounds [5,6].

Pharmaceutical wastewaters are usually treated using biological [7], physical [8], and chemical methods, as well as combinations of them [9]. Advanced Oxidation Processes

(AOPs) including advanced oxidation based on ultraviolet–visible [10], natural sunlight [11], electrochemical [12], Fenton oxidation [13], sonolysis, and sono-Fenton [14] have been widely used to remove pollutants from pharmaceutical wastewaters, delivering excellent results. Those are related to the formation of highly oxidizing radicals during these processes. In comparison to other methods, photocatalysis offers several advantages, such as high efficiency, corrosion, and temperature stability [15] and low cost [16]. Photocatalytic treatment is the technology of choice for the degradation of pollutants in air and water. Photocatalysis belongs to the broader field of heterogeneous catalysis; it is essentially a surface phenomenon using semiconductors such as titanium dioxide (TiO_2), known for their oxidizing properties under ultraviolet (UV). The free radicals released by titania allow oxidation reduction: the organic molecules present on the treated surface are adsorbed and decomposed by the catalyst. Semiconductor metal oxides have also been proven to be very effective catalysts in the field of photocatalysis [16].

Titanium dioxide, as an inert compound that is photo-stable in water and air, inexpensive, abundant, and non-toxic [17], remains the raw material chosen by most manufacturers. In the degradation of pharmaceutical pollutants and organic compounds, as it is a light-sensitive semiconductor [18,19], it can easily degrade organic compounds into non-toxic ones such as CO_2 and water. There are several types of TiO_2: Rutile, Anatase, and Brookite, but in photocatalysis, only Rutile and Anatase are used on the performance side, with Anatase being generally more active than Rutile [20,21]. This difference is due to several factors: particle size, specific surface, surface content of $OH^\bullet$, adsorption of UV photons, and mobility of charges generated within TiO_2 [22,23].

Furthermore, solar photocatalysis is particularly interesting for the elimination of pollutants using solar energy as the only source of energy, saving operating costs and making it a possible route for implementation in industry or in the tertiary treatment of a wastewater treatment plant [22]. Thus, the use of solar energy is presented as a sustainable alternative since the cost of installing and operating AOPs is relatively high. However, the high band gap of TiO_2 (3.0–3.2 eV) limits the application of solar radiation because only the ultraviolet (UV) region of the solar spectrum can be utilized by titanium dioxide for the photogeneration of electron–hole pairs, resulting in low use of solar energy (less than 5%) and, consequently, low activity [22]. The combination of TiO_2 with other metal oxides is effective in creating an extension of the field of action in the visible region, and the transfer of photogenerated charges between the chosen semi-conductor and TiO_2 can limit the phenomena of recombination of electron–hole pairs and create synergy, therefore improving the activity of TiO_2 [16,24–26]. S.M. Thabet et al. [25] demonstrated that the loading of metal co-catalysts (Ru, Co, and Ni) into TiO_2 nanoparticles significantly improved the photocatalytic activity of titanium dioxide toward hydrogen generation. In turn, L. Li et al. [26] showed that CuO_x/TiO_2 composites exhibited a unique structure, which exhibited excellent photodegradation performance toward rhodamine B (RhB) under visible-light illumination. The Ti^{3+} defects in the Ti^{3+}/TiO_2 substrate altered the valence state of the Cu atoms, which facilitated the transfer of photogenerated electrons from the TiO_2 conduction band (CB) to the CuO_x species.

Together, TiO_2 along with other metal oxides (ZrO_2, ZnO, SnO_2, CeO_2, etc.) have proven their photocatalytic effectiveness in degrading a wide range of pollutants into biodegradable compounds and ultimately mineralizing them into harmless carbon dioxide and water. Among them, the photoactivity of zirconium oxide is associated with its n-type semiconductor nature, showing good performance in degrading different pollutants [23,27]. However, photocatalytic activity was not obtained under visible light since the value (5.1 eV) reported for the band gap energy of this oxide is high [28]. Nevertheless, this parameter can be lowered significantly depending on the preparation (sol–gel, precipitation, hydrothermal, etc.) [29], thus improving its potential use as a photocatalyst.

ZrO_2 has been used by several authors to increase the photocatalytic activity of TiO_2 toward dye removal [30–32]. Indeed, the coupling of the two semiconductors makes it possible to obtain more efficient charge separation and prolong the duration of life of the

charge carriers, increasing the specific area and significantly decreasing the probability of combination between the hole and the electron [33–36]. Zirconium and titanium-based materials were previously used in photocatalysis by some authors. Polisetti et al. [28] studied the activity of ZrO_2 and ZrO_2-TiO_2 mixed oxides synthesized by the solution combustion technique in the photocatalytic degradation of dyes and obtained around 50% degradation after 120 min of photocatalytic reaction under UV irradiation. Binitha et al. [30] studied the photodegradation of methyl orange under direct solar irradiation for 180 min using zirconium-doped titania-based photocatalysts prepared by the sol–gel method and achieved around 80% degradation. Bailon Garcia et al. [32] also investigated the degradation of Orange G dye under visible irradiation using Carbon-ZrO_2 composites prepared by the sol–gel method; total degradation was obtained after 300 min of treatment. Li et al. [37] studied the photocatalytic degradation of Sulfamethoxazole using Cerium Zirconium Oxide Nanocomposites prepared by the hydrothermal method and found that the best was $Ce_{0.9}Zr_{0.1}O_2$ with 91% degradation. Ding et al. [38] studied the photodegradation of berberine hydrochloride under visible light irradiation using TiO_2/ZrO_2/g-C_3N_4 composites prepared by the hydrothermal method and they obtained 85% degradation. Aguirre-Cortes et al. [39] synthesized TiO_2-ZrO_2 nanoparticles using the two-emulsion method, obtaining SMX degradation of 80% after 550 min under visible light. However, tedious, expensive, or non-environmentally friendly methods using organic solvents such as Heptane were used for the synthesis of the materials.

In this paper, the materials ZrO_2-TiO_2 and TiO_2-ZrO_2 with molar ratios of 75–25% were prepared by the sol–gel method, which is a facile, low-cost, environmentally friendly method. The physico-chemical properties of these composites have been studied in order to optimize their catalytic performances. These materials were tested in the photodegradation of polluted water under UV irradiation and visible light. Sulfamethoxazole (SMX), a sulfonamide antibiotic usually used to treat urinary tract infections, toxoplasmosis, and sinusitis [40], was used as a model molecule since it is currently the fourth most widely used antibiotic globally. In recent years, high concentrations of SMX have been detected in wastewater effluents from the pharmaceutical industry. The presence of SMX in water can disrupt essential bacterial cycles crucial to aquatic ecosystems, promote antibiotic resistance in microorganisms, and pose risks to human health. Consequently, there is an urgent need to remove this antibiotic in conventional water treatment processes. The ability of our materials to photodegrade this antibiotic was studied, and the relationship between photocatalytic activity and physico-chemical properties was established.

2. Results and Discussion

2.1. Thermogravimetric Analysis

These analyses make it possible to measure the losses and gains in mass of a sample as a function of the increase in temperature. Differential and gravimetric analyses for uncalcined samples are represented in Figure S1. For the two materials, ZrO_2-TiO_2 and TiO_2-ZrO_2, similar profiles were obtained, with a mass loss of approximately 22% between room temperature and 400 °C, which is due to the dehydration of the water and alcohol adsorbed on the external surface at the lowest temperatures and the elimination of residual water that may remain in the precursors at the higher temperatures [41]. A small gain of mass is observed after 400 °C, which could be attributed to a possible rearrangement of the TiO_2/ZrO_2 structure or the formation of an amorphous to thermodynamically stable anatase crystal phase, leading to some oxygen inclusion from the air [41,42].
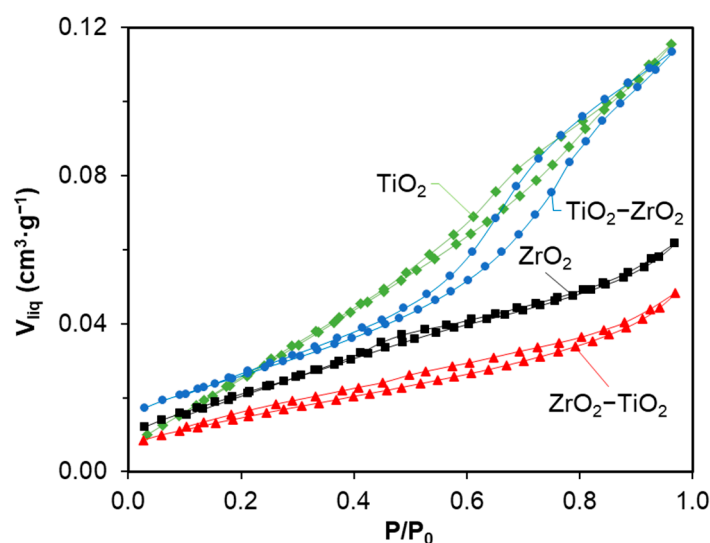
2.2. Nitrogen Adsorption–Desorption

Textural properties are very important in the analysis of the photocatalytic performance of materials. Thus, the texture characteristics of titania/zirconia-based materials were examined using nitrogen adsorption/desorption analysis. The detailed textural results of specific surface (S_{BET}), micropore (V_{micro}) and mesopore (V_{meso}) volumes, and pore size (L_0) are listed in Table 1 and the isotherms and pore size distribution are included

in Figure 1. All samples present type II-IV isotherms characteristic of meso-macroporous materials where the defined hysteresis loop manifests as the presence of mesoporosity. Research has revealed that a pore size larger than 2 nm is suitable for facilitating the reactants' penetration into the porous structure of the photocatalyst [43]. The specific surface area of ZrO_2 was 54 $m^2 \cdot g^{-1}$ and increased to 64 $m^2 \cdot g^{-1}$ after the incorporation of TiO_2. For TiO_2, it was 90 $m^2 \cdot g^{-1}$, which became 37 $m^2 \cdot g^{-1}$ after the incorporation of ZrO_2. So, the hydrolysis of the titania precursor into the previously synthesized ZrO_2 creates new mesoporosity whereas the incorporation of ZrO_2 into TiO_2 conversely produces a blockage of the porosity. The results show that the preparation of mixed oxides using the sol–gel method, especially TiO_2-ZrO_2, led to the improvement of textural properties, which can improve photocatalytic properties whereby adding 75% of TiO_2 means the mesopore volume is as high as that for pure TiO_2.

Table 1. Textural properties of materials.

Materials	S_{BET} (m^2g^{-1})	V_{micro} (cm^3g^{-1})	V_{meso} (cm^3g^{-1})	L_0 (nm)
TiO_2	90	0.029	0.087	3.86
ZrO_2	54	0.022	0.040	2.81
ZrO_2-TiO_2	37	0.015	0.033	2.68
TiO_2-ZrO_2	64	0.027	0.087	2.40

Figure 1. N_2−adsorption isotherms of samples.

2.3. Scanning Electron Microscopy

The morphology of the samples was analyzed using a scanning electron microscope and the results are represented in Figure 2. For all materials, large spherical particles (around 100–500 nm) were observed to coexist with much smaller ones. The average particle size calculated from the analysis of the SEM images with the software ImageJ (V1.8.0) was 160, 149, and 88 nm for TiO_2, ZrO_2-TiO_2, and TiO_2-ZrO_2, respectively. Note from the particle size histogram that most of the particles were around 30–100 nm for TiO_2 and ZrO_2-TiO_2, whereas smaller particles with a size lower than 30 nm were obtained for TiO_2-ZrO_2 and ZrO_2 samples. Homogeneous particles with sizes smaller than 30 nm were also observed by HRTEM for TiO_2-ZrO_2 (Figure 2f), and HAADF (Figure 2g) and EDX mapping (Figure 2h) showed intimate contact between TiO_2 and ZrO_2 particles.
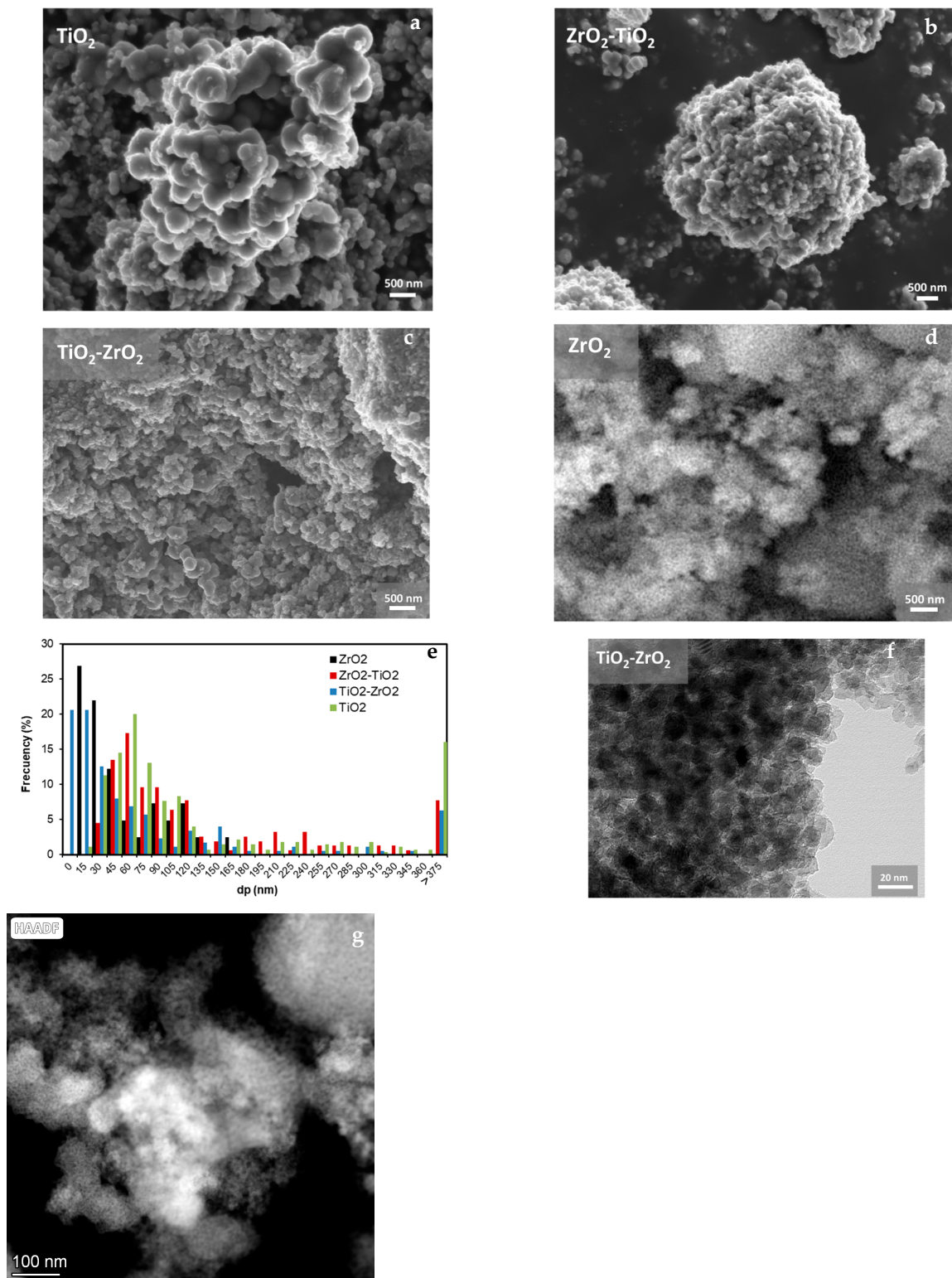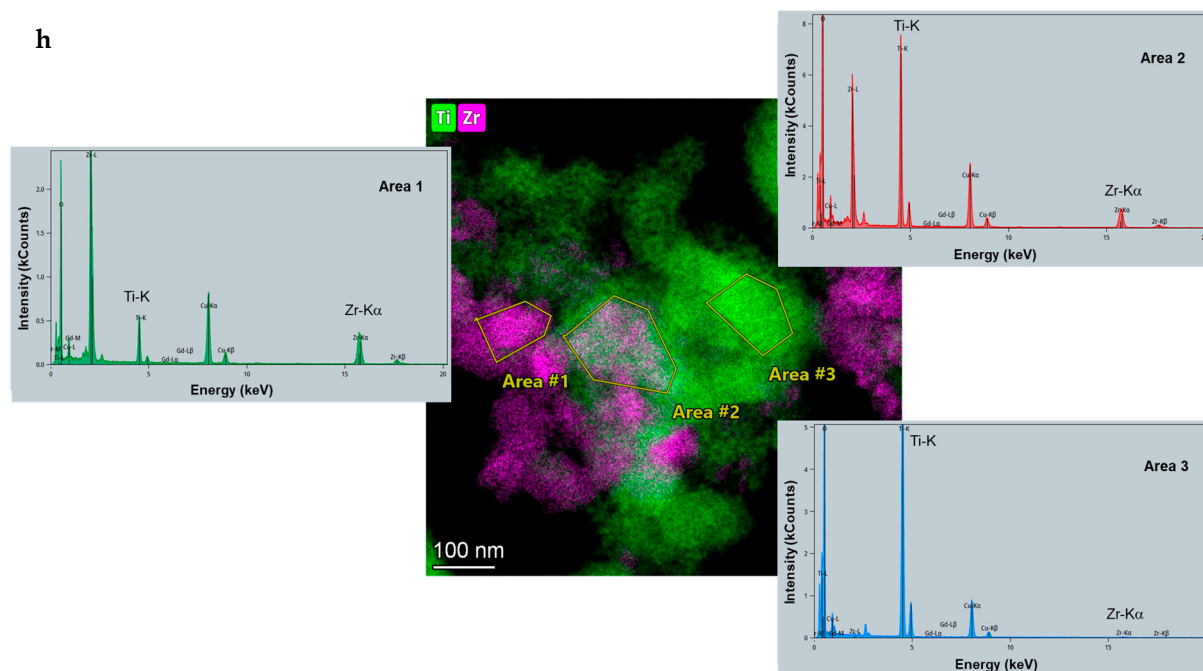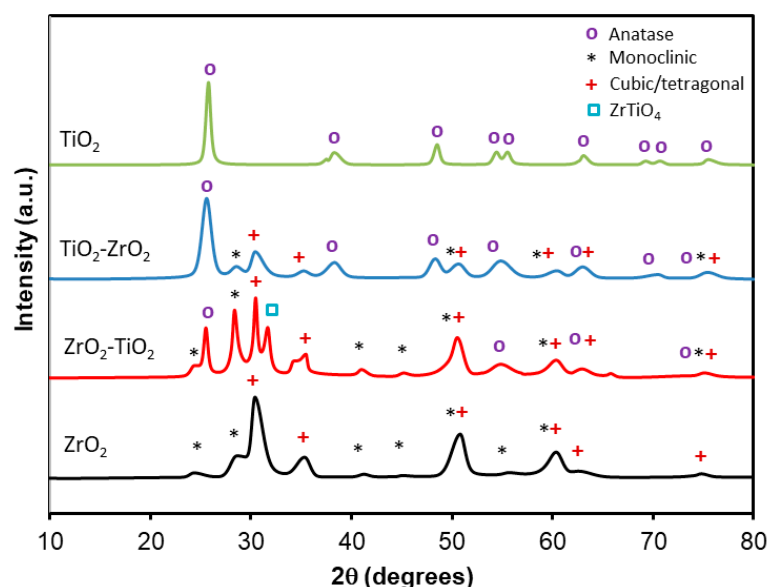
Figure 2. *Cont.*

Figure 2. (**a**–**d**) SEM images showing the morphology of samples. (**e**) Particle size distribution obtained by SEM. (**f**) HRTEM image. (**g**) HAADF image and (**h**) EDX mapping of TiO_2-ZrO_2.

2.4. X-Ray Diffraction

XRD was used to study the crystallinity of the samples (Figure 3) and calculate the average crystallite size (dp) using the Scherrer formula.

Figure 3. Powder XRD patterns of samples.

The TiO_2 pattern shows characteristic peaks of the Anatase phase at $2\theta = 25.28°$, $38.57°$, $48.05°$, $54.06°$, $55.49°$, $62.69°$, $69.14°$, $70.77°$, and $75.03°$ corresponding to the (101), (112), (200), (105), (211), (204), (116), (220), and (215) crystallographic planes, respectively [44–47].

The ZrO_2 pattern shows peaks at $2\theta = 24.54°$, $28.62°$, $41.18°$, $50.37°$, $55.5°$, $60.6°$, and 74,8 corresponding to (011), (111),(211), (022), (130), and (311) planes of the monoclinic phase [44,48–51] and peaks at $2\theta = 30.36°$, $35.3°$, $50.37°$, $60.61°$, $62.70°$, and $74.5°$ corre-

sponding to the (101)/(111), (002)/(200), (112)/(220), (211)/(311), (202)/(222), and (400) crystallographic planes of the tetragonal/cubic phase, respectively [32,44,45,48–51].

The patterns of ZrO_2-TiO_2 and TiO_2-ZrO_2 show the characteristic peaks of Anatase TiO_2 as well as those of monoclinic and tetragonal/cubic ZrO_2 [32,44,49]. A difference in intensity of ZrO_2 and TiO_2 peaks is noted in ZrO_2-TiO_2 and TiO_2-ZrO_2 samples; in ZrO_2-TiO_2, ZrO_2 peaks are more intense, whereas for TiO_2-ZrO_2, the opposite is observed, which is ascribed to the difference in the percentages of the two materials. It is important to highlight the appearance of a new peak at $2\theta = 32°$ in the ZrO_2-TiO_2 sample, which corresponds to the (100) crystalline plane of $ZrTiO_4$ [52].

According to the literature, it is difficult to distinguish the tetragonal/cubic phases of ZrO_2 by XRD because they have similar lattice parameters and peak broadenings $a_0 = 0.5094$ nm and $c_0 = 0.5177$ nm for tetragonal structures and $a_0 = 0.5124$ nm for the cubic structure [50,53]. However, it has been reported that the stability of different ZrO_2 particles strongly depends on the crystal size [32,51]. Several authors have observed that the cubic phase could be stabilized at a particle size below 6 nm [32]. The tetragonal phase is found to be stable at a particle size above 6 nm and below 20 nm. The crystal size of each phase for all samples was calculated by applying the Scherrer equation to the more intense peak of this phase, and the results are included in Table 2. Note that the approximate crystal dimensions for ZrO_2 (tetragonal or cubic) were 6 nm for ZrO_2 and TiO_2-ZrO_2 while it was 11 nm for ZrO_2-TiO_2. Thus, in this case, it seems that tetragonal ZrO_2 was obtained in ZrO_2-TiO_2, whereas tetragonal or cubic ZrO_2 could be stabilized in pure ZrO_2 and TiO_2-ZrO_2. The dp of pure ZrO_2 (both phases) and TiO_2 was 6 and 14 nm, respectively. This size was not modified after the addition of the coupled semiconductor for mixed oxides prepared by the addition of the oxide precursor onto ZrO_2 and TiO_2 previously synthesized particles (6 and 14 nm, respectively). Conversely, the size of the oxide hydrolyzed in the presence of titania or zirconia was affected and depended on the oxide present in the solution. If TiO_2 precursor is added to ZrO_2, the particle size of Anatase decreases from 14 nm to 7 nm, whereas for the ZrO_2 precursor, the trend is the opposite, whereby the particle size of zirconia increases from 6 nm to 11–12 nm.

Table 2. Molar fractions of phases, crystallite size (dp), and d-spacing of the samples determined by XRD.

Sample	Crystal Phase	Molar Fraction (%)	dp (nm)	d-Spacing (nm)
TiO_2	Anatase	100	14	0.345
ZrO_2	Tetragonal/cubic	78	6	0.294
	Monoclinic	22	6	0.312
TiO_2-ZrO_2	Anatase	100	7	0.349
	Tetragonal/cubic	51	6	0.294
	Monoclinic	49	6	0.312
ZrO_2-TiO_2	Anatase	100	14	0.349
	Tetragonal/cubic	51	11	0.293
	Monoclinic	49	12	0.313

To determine the possible insertion of Ti or Zr cations on the ZrO_2 or TiO_2 structure, respectively, the d-spacing was calculated using the Bragg law. The d-spacing of pure Anatase TiO_2, m, and c/t ZrO_2 were 0.354, 0.312, and 0.294 nm, respectively, which are consistent with the values stated for these pure phases [54–57]. The insertion of cations of different sizes produces lattice distortions, increasing or decreasing the unit cell parameter if the cations are higher or lower in size. Since the cation size of Zr^{4+} (0.072 nm) is fairly higher than that of Ti^{4+} (0.061 nm) [58], the cell parameter of titania should increase if Zr ions are introduced to its structure and the cell parameter of zirconia should decrease if Ti ions are introduced to its structure. Note that the cell parameter of zirconia remains unchanged (Table 2) in both mixed oxides, which means that Ti cations are likely not

introduced into the zirconia structure. However, the lattice parameter of titania increases from 0.345 to 0.349 nm in both mixed oxides, which denotes the insertion of Zr cations into the titania structure.

The molar fractions of the monoclinic (X_m) and cubic/tetragonal (X_t) phases (Table 2) were estimated using the Toraya equation [50,59].

$$X_m = \frac{I_{m\ (-111)}}{I_{m\ (-111)} + I_{t\ (101)}} \tag{1}$$

$$X_t = \frac{I_{t\ (101)}}{I_{m\ (-111)} + I_{t\ (101)}} \tag{2}$$

where $I_{m\ (-111)}$ is the intensity of monoclinic ZrO_2 peak at 28.62° and $I_{t(101)}$ is the intensity of tetragonal ZrO_2 peak at $2\theta = 30.36°$.

The results show the presence of a 22% monoclinic phase and a 78% tetragonal/cubic phase for pure ZrO_2. These findings align with the literature, elucidating that the formation of tetragonal/cubic and monoclinic phases is linked to the calcination temperature; below 400 °C, the tetragonal phase predominates, while above 400 °C, the formation of monoclinic phases begins [60,61]. However, in both mixed oxides, the amount of monoclinic phase increases to 49% (vs. 22% for pure ZrO_2), suggesting that the presence of titania may promote the stabilization of the monoclinic phase.

2.5. UV-Vis Spectroscopy

UV-Vis diffuse reflectance spectra were recorded to study the optical properties of samples and the Kubelka–Munk theory was applied to calculate the band gap (E_g) of samples. For that, $(F^® • hv)^{0.5}$ was plotted as a function of hv (Figure 4). It is well known that the band gap value of ZrO_2 depends on the crystal structure. The reported calculated band gaps of monoclinic, tetragonal, and cubic phases are 4.51, 4.11, and 3.84 eV, respectively [62], while the experimental data reported are usually higher at 5.8, 4–5, and 3–4 eV [62,63]. In our case, the band gap obtained for pure zirconia was 4.90 eV, which can indicate that the cubic phase is not obtained, but rather the tetragonal phase is. This result agrees with the XRD where cubic/tetragonal characteristics peaks were detected as the major phase and the crystal size indicated the prevalence of the tetragonal phase. The band gap of pristine Anatase titania was 3.20 eV, as was previously reported in the literature [64].
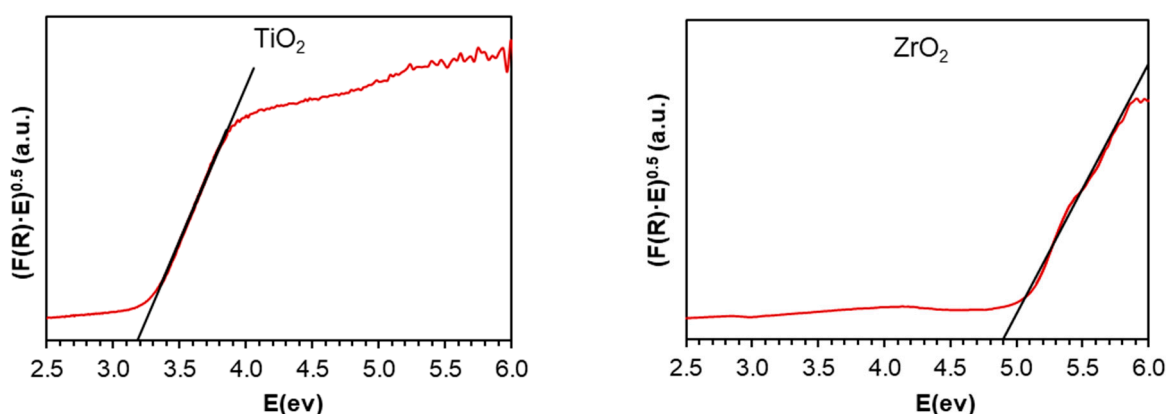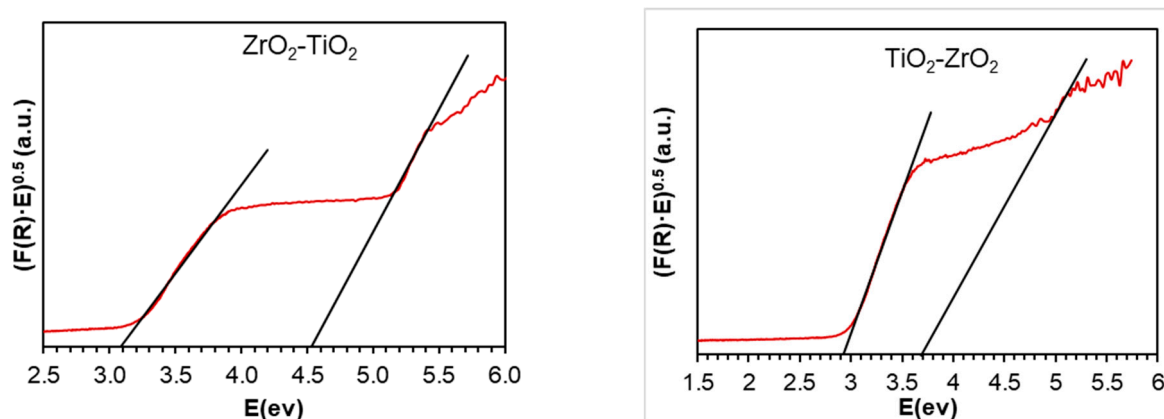

Figure 4. *Cont.*

Figure 4. Diffuse reflectance spectra of samples.

In mixed oxides, two defined steps are observed: one at low values and another at higher band gap values attributed to TiO_2 and ZrO_2, respectively. Note that the intensity of this step is different in both mixed oxides. In ZrO_2-TiO_2, the zirconia step is more pronounced and the titania step is less pronounced than that of TiO_2-ZrO_2, which is due to the quantity of both phases, with 75% ZrO_2-25% TiO_2 in the first and 25% ZrO_2-75% TiO_2 in the last one. Moreover, the band gaps of both phases are shifted in both mixed oxides. The titania band gap decreases from 3.20 to 2.93 eV when titania is added to zirconia and 3.08 eV when zirconia is added to titania. This band gap decrease can be attributed to Zr-Ti heterojunction/titania doping with the formation of zirconium titanate due to the presence of the zirconia phase. Similarly, the band gap of zirconia decreases from 4.90 eV to 4.52 eV when zirconia is added to titania (ZrO_2-TiO_2) and 3.68 eV when titania is added to zirconia (TiO_2-ZrO_2). Similarly, two direct regions have been observed in the thin films of ZrO_2 [65] and thin films of FeS_2 [66]. The authors explained that these materials have a tail band, which means that there is a high structural disorder in the solid due to an excess of oxygen. This is what explains the decrease in the energy gap. This disordered structure may be a result of the conditions used in the preparation technique. Due to structural defects, some energy levels are introduced into the semiconductor band gap, which allows transitions of lower energy and then leads to a decrease in the band gap energy [65,67].

In our case, according to the XRD results, structural defects led to the formation of a new crystalline phase $ZrTiO_4$ (Figure 3). However, according to the literature [49], it could also be $ZrO_{0.35}$, which appears at $2\theta = 22°$ and $25.4°$ but might be covered by the monoclinic diffraction peak at $2\theta = 25.4°$. These results indicate that our materials demonstrate efficiency and hold promise for yielding favorable outcomes in photocatalysis.

2.6. FTIR Spectroscopy

The Fourier transform infrared (FTIR) spectrophotometry spectra characteristics of the materials are recorded in the range of 4000 to 600 cm^{-1} and presented in Figure 5.

The results show shoulders in the spectra of ZrO_2-TiO_2 and TiO_2-ZrO_2 around 500–800 cm^{-1} associated with Ti–O and Zr–O vibrations [68,69]. The bands at 1043 and 1114 cm^{-1} could be assigned to the vibrations of coordinated carbonate ions resulting from the adsorption of carbon dioxide after exposure to the atmosphere [70,71]. These peaks are observed in mixed oxides where the introduction of Zr cations into the titania structure creates a more defective surface with more reach in oxygen vacancies (see XPS) able to perform CO_2 chemisorption [72,73]. The peaks present in all samples located at 1600 cm^{-1} are attributed to the H–O–H stretching modes of the hydroxyl group [68–74]. The band at 2300–2400 cm^{-1} is associated with the presence of adsorbed CO_2. The bands at 2880 and 2980 cm^{-1} are attributed to the stretching vibrations of C–H bonds in CH_2 and CH_3 [68], while the broad band around 3272 cm^{-1} present in mixed materials corresponds to the

bending vibrations of the –OH groups attached to the water interlayer adsorbed by the surface [12,74].
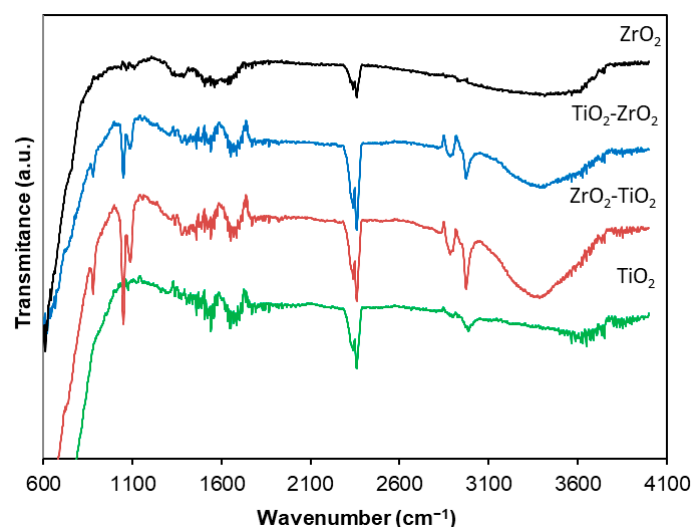
Figure 5. FTIR spectra of samples.

2.7. X-Ray Photoelectron Spectroscopy

The surface chemistry of the samples was studied by XPS, and the O_{1s}, Ti_{2p}, and Zr_{3d} spectral regions are presented in Figure 6. Three peaks are required to deconvolve the O_{1s} region (Figure 6a) assigned to lattice oxygen (O_{lat}) at 529.8 eV, adsorbed oxygen on surface oxygen vacancies (O_{ads}) at 531.1 eV, and C-O species at 532.5 eV [75,76].

The mixed oxides present a higher content of O_{ads} than the TiO_2 sample, denoting more defective surface/oxygen vacancies. It is important to highlight that the TiO_2-ZrO_2 sample presents an approximately 71% contribution to this peak as it is the one with the highest contribution of all samples. This indicates an oxygen vacancy-rich surface in this sample. This more defective surface is also pointed out by analyzing the Ti_{2p} region (Figure 6b). One peak at 459.9 eV is observed for the pure TiO_2 sample in the $Ti_{2p3/2}$ region attributed to Ti^{4+}. This peak is displaced to lower binding energy for mixed oxides, denoting an electron-rich environment of Ti^{4+} species. A new peak appears at 457.6 eV for the TiO_2-ZrO_2 sample, which can be ascribed to Ti^{3+}/zirconium titanates species [39], corroborating the more defective surface of this sample. Since the XPS is a superficial technique in which the more external surface is analyzed, this peak may not appear in ZrO_2-TiO_2 because titanates are not superficial enough or the surface quantity is not high enough for a good signal. Since this peak is also related to oxygen vacancies/Ti^{3+}, this indicates a more defective surface of the TiO_2-ZrO_2 sample in comparison with the other ones.

Regarding the $Zr_{3d5/2}$ region, two peaks are observed at 181.6 eV and 182.6 eV for pure ZrO_2, which are ascribed to Zr^{+4} in stoichiometric ZrO_2 and non-stoichiometric oxides (ZrO_y: $0 < y < 2$), respectively [77]. Two peaks are also required to deconvolve the $Zr_{3d5/2}$ region of the mixed-oxide samples, but the relative intensity of both peaks is different. The contribution of this non-stoichiometric oxide peak was 47.3, 19.6, and 55.8% for ZrO_2, ZrO_2-TiO_2, and TiO_2-ZrO_2, respectively. Thus, the TiO_2-ZrO_2 sample presents a more defective surface, as is denoted by the higher contribution of O_{ads}, Ti^{3+}, and ZrO_y species, which could explain the lower band gap obtained for this sample.
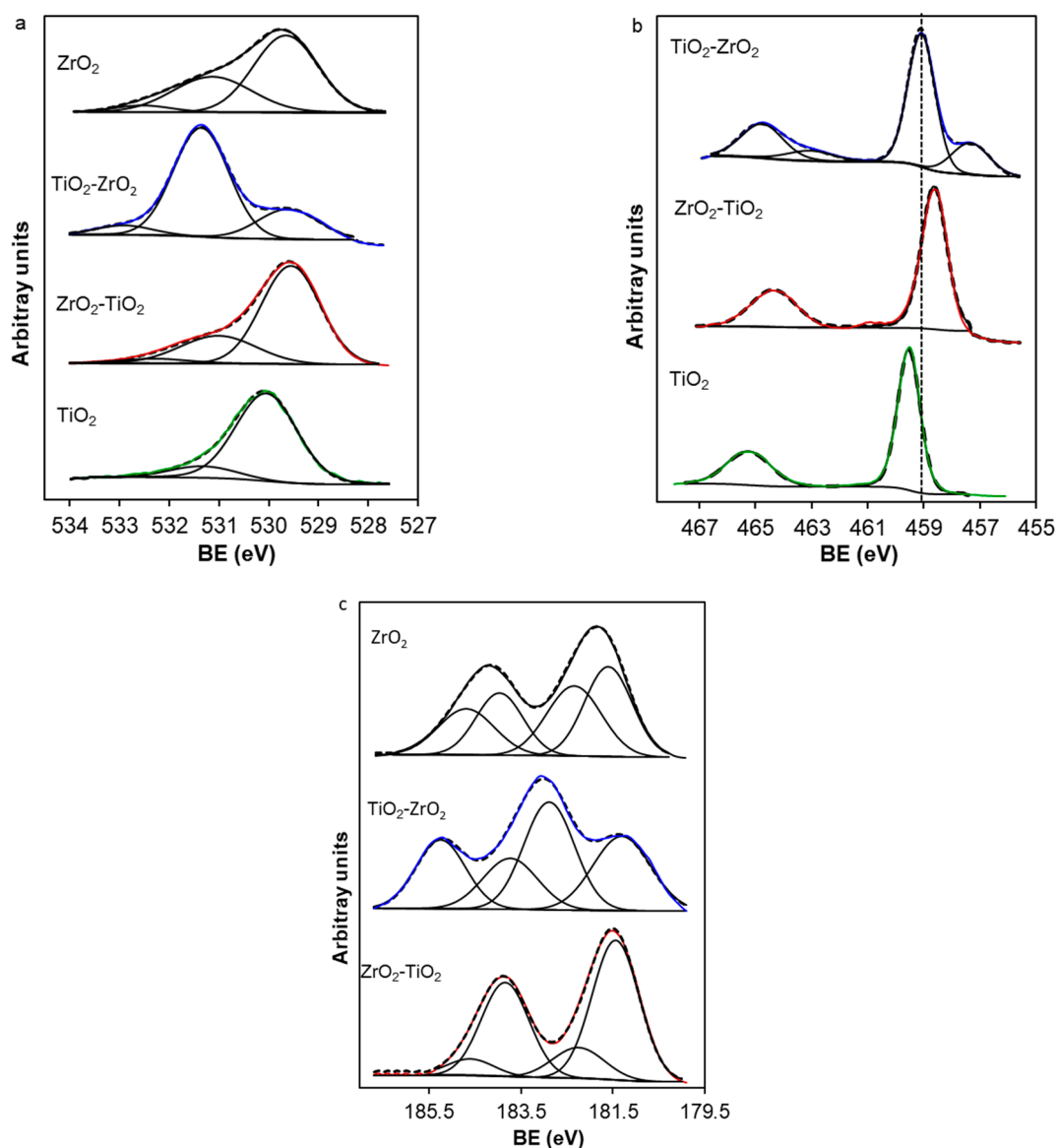
Figure 6. XPS spectra: (**a**) O_{1s}, (**b**) Ti_{2p}, and (**c**) Zr_{3d}.
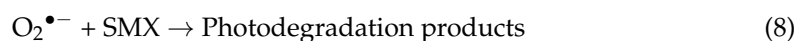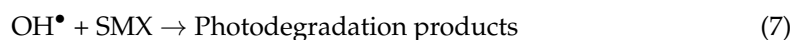
2.8. Photocatalytic Reaction

The photocatalytic activity of the materials was evaluated using the sulfamethoxazole (SMX) antibiotic as a model wastewater pollutant under two types of irradiation: UV lamp and blue LED light. Pure ZrO_2 and TiO_2 were used as reference materials. Before the catalytic test, the solution pH was adjusted to 7 to be sure that the same conditions were maintained, and the catalyst was saturated with the pollutant in the dark in order to avoid adsorption interferences; the concentration after saturation was fixed at 12 mgL^{-1}.

Figure 7 illustrates the degradation of SMX in terms of irradiation time under UV (a) and blue LED irradiation (b). The ZrO_2, TiO_2, ZrO_2-TiO_2, and TiO_2-ZrO_2 catalysts showed the total degradation of SMX after 480 min, 360 min, 240 min, and 120 min, respectively. Under blue LED irradiation, the degradation percent after 480 min was 18%, 35%, 37% and 76%, respectively.
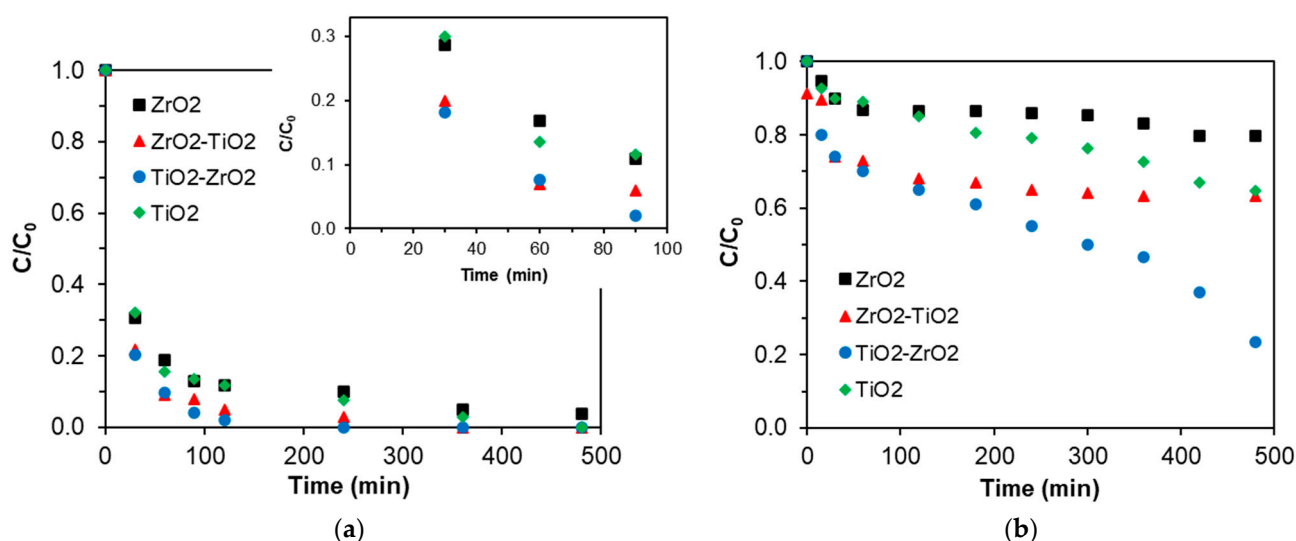
Figure 7. (**a**) Kinetics of SMX photocatalytic degradation under UV irradiation; (**b**) kinetics of SMX photocatalytic degradation under blue LED irradiation.

In the literature, the process of photocatalytic degradation of SMX over catalysts can be described as follows [22,49]: The first step requires the adsorption of the pollutant onto the surface of the sample. The exposure of the drug adsorbed by the particles in the presence of blue LED or UV irradiation leads to the generation of electron–hole (e–h+) pairs in the catalysts, as indicated in Equation (3). The photogenerated electrons in the catalyst's conduction band interact with the oxygen molecules adsorbed to form superoxide anion radicals ($O_2^{\bullet-}$) (Equation (4)). The holes generated in the material's valence band react with surface hydroxyl groups to produce highly reactive hydroxyl radicals (Equation (5)). These photogenerated holes can lead to the dissociation of water molecules in the aqueous solution, producing radicals (Equation (6)). The highly reactive hydroxyl radicals ($OH^{\bullet}$) and superoxide radicals ($O_2^{\bullet-}$) can react with SMX adsorbed on the catalyst particles and lead to its degradation, as represented by Equations (7) and (8).

$$\text{Catalyst} + h\upsilon \rightarrow e^- + h^+ \tag{3}$$

$$O_2 + e^- \rightarrow O_2^{\bullet-} \tag{4}$$

$$h^+ + OH^- \rightarrow OH^{\bullet} \tag{5}$$

$$h^+ + H_2O \rightarrow H^+ + OH^{\bullet} \tag{6}$$

$$OH^{\bullet} + \text{SMX} \rightarrow \text{Photodegradation products} \tag{7}$$

$$O_2^{\bullet-} + \text{SMX} \rightarrow \text{Photodegradation products} \tag{8}$$

Under UV light, similar degradation activity is obtained for pure TiO_2 and ZrO_2 (89% at 120 min). The zirconium oxide prepared by the simple, economical, and eco-friendly sol–gel method produced interesting results that can be ascribed to the presence of a tetragonal phase, which was reported to have enhanced photocatalytic properties [78,79]. However, under blue LED light, poor degradation was obtained for pure ZrO_2 and TiO_2 ascribed to the highest band gap of these solids, which limits the activity under visible light yet is still an interesting result compared to other studies [80,81].

Higher activity was obtained for the mixed oxides under both types of irradiations regarding pure oxides. However, a significant difference was observed in the photocatalytic activity between ZrO_2-TiO_2 and TiO_2-ZrO_2, which can first be explained by the difference in the molar quantity of titanium dioxide, which is higher in TiO_2-ZrO_2 (75%) than ZrO_2-TiO_2 (25%). Secondly, it is well known that the photocatalytic activity depends on the adsorption capacity of the photocatalyst, and the adsorption capacity increases with surface area and

specific interactions. The activity is highly improved as a result of the improvement of the surface area, electrostatic interactions [82], pore size, and volume [49]. The higher surface area and mesopore volume of TiO_2-ZrO_2 explains the big difference between ZrO_2-TiO_2 and TiO_2-ZrO_2. Another important factor of photocatalytic activity improvement is the gap energy, which was lower for both materials (2.93 eV for TiO_2-ZrO_2 and 3.08 eV for ZrO_2-TiO_2) and resulted in better activity in visible light.

Another key factor to take into account in organic pollutant photocatalytic degradation is the degree of pollutant mineralization since intermediates could pose greater risks than the original pollutant. The mineralization rates of SMX under blue LED were evaluated by measuring the total organic carbon concentration at the initial (TOC_0) and final times (TOC) (Figure 8). Note that mineralization rates follow the same trend as the degradation rates, with the TiO_2-ZrO_2 samples obtaining the highest mineralization rate. Nonetheless, since the mineralization of the pollutant is not complete, a toxicity study was carried out using Vibrio Fischeri bacteria for the more active sample. The results are shown in Figure 8. The toxicity curve is very similar to the pollutant degradation curve. This fact indicates that the photodegradation of SMX simultaneously leads to a decrease in the polluted water's toxicity.
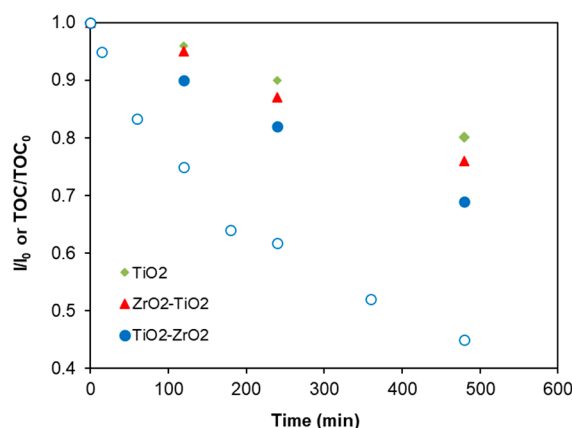
Figure 8. Variation of the total organic carbon concentration and toxicity of solution treated with the synthesized photocatalysts. Close symbol: TOC/TOC_0; open symbol: I/I_0.

According to these results and comparing them to other similar works (Table 3) where either the photocatalysts were prepared with complicated, expensive, or not ecological methods or the photocatalytic reaction was carried out using simple pollutants like dyes and under UV lamps, the sol–gel method used in this work is an interesting method to synthesize photocatalysts for the visible-light degradation of wastewater drugs.

Table 3. Comparison with similar studies in literature.

Catalyst	Catalyst Preparation	Pollutant	Conditions	% Degradation	Ref
Monoclinic ZrO_2 Tetragonal ZrO_2 Cubic ZrO_2	Sol–gel Precipitation-colloidal Hydrothermal	MO	UV; 110 min; Cat. 100 mg/100 mL; Dye 10 ppm	99% 90% 80%	[49]
TiO_2 thin film	Commercial TiO_2	SMX	UV; 420 min; Cat. 400 mg/100 mL; SMX 10 ppm;	97%	[80]

Table 3. *Cont.*

Catalyst	Catalyst Preparation	Pollutant	Conditions	% Degradation	Ref
Biochar supported TiO$_2$	Sol–gel	SMX	UV; 360 min; Cat. 500 mg/100 mL; SMX 10 ppm;	91%	[81]
F-Pd co-doped TiO$_2$	microwave-assisted hydrothermal	SMX	Solar; 70 min; Cat.50/50 mL; SMX 30 ppm;	98%	[83]
ZrO$_2$-TiO$_2$	Solution combustion technique	OG	UV; 120 min; Cat. 1 g/L; OG 100 ppm	22%	[28]
		AB	UV; 90 min; Cat. 1 g/L; AB 100 ppm	50%	
		RBBR	UV; 120 min; Cat. 1 g/L; RBBR 100 ppm	60%	
		ACG	UV; 120 min; Cat. 1 g/L; ACG 100 ppm	52%	
ZrO$_2$ TiO$_2$ ZrO$_2$-TiO$_2$ TiO$_2$-ZrO$_2$	Sol–gel	SMX	Blue LED; 480 min; Cat. 1 g/L; SMX 12 ppm	18% 30% 38% 76%	current work
ZrO$_2$ TiO$_2$ ZrO$_2$-TiO$_2$ TiO$_2$-ZrO$_2$	Sol–gel	SMX	UV; 480 min; Cat. 1 g/L; SMX 12 ppm	100% 100% (360 min) 100% (240 min) 100% (120 min)	current work

MO: methyl orange; SMX: sulfamethoxazole; OG: Orange G; AB: Amido Black; RBBR: Remazol Brilliant Blue R; ACG: Alizarin Cyanine Green.

3. Materials and Methods

3.1. Chemicals

The products used are from Sigma Aldrich: Titanium isopropoxide (Ti[OCH(CH$_3$)$_2$]$_4$, 97%), Tetrapropylzirconate (Zr(OCH$_2$CH$_2$CH$_3$)$_4$, 70%), Propanol (CH$_3$CH$_2$CH$_2$OH, 99%), Ammonia (NH$_4$OH, 33%), and Sulfamethoxazole (C$_{10}$H$_{11}$N$_3$O$_3$S).

3.2. Catalyst Preparation

3.2.1. Simple Oxides

Titanium dioxide was prepared by mixing solution S1 containing 0.031 mol of ammonia, 1.58 mol of water, and propanol as the solvent with solution S2 containing 0.1 mol of Titanium isopropoxide and propanol as the solvent. The mixture (S1 and S2) was stirred for 6 h at 60 °C and then aged for 16 h at room temperature. After drying for 8 h at 80 °C, the material was calcined for 1 h at 500 °C (with an increasing temperature of 3 °C min^{-1}). Zirconium oxide was prepared following the same method where 0.05 mol of tetrapropylzirconate was used.

3.2.2. Mixed Oxides

Molar ratios of 75% TiO$_2$-25% ZrO$_2$ and 25% TiO$_2$-75 ZrO$_2$ were studied in this manuscript. In previous works [39,77], TiO$_2$-ZrO$_2$ materials were prepared using more tedious, more expensive, and less eco-friendly methods and tested as photocatalysts under visible light, obtaining an optimal ratio of around 75 TiO$_2$-25 ZrO$_2$. For this reason, this molar ratio was selected for this eco-friendlier route. In order to synthesize ZrO$_2$-TiO$_2$ with a molar ratio (75–25%), 0.01 mol of TiO$_2$ was dispersed in water and stirred for 24 h at room temperature. Next, 0.08 mol of tetrapropylzirconate solubilized in propanol was added (which led to 0.03 mol of ZrO$_2$). The pH was adjusted at 3 using dropwise HCl (0.1 M), and

then the solution was stirred for 24 h at 60 °C. The sample was dried for 8 h at 80 °C and finally calcined for 2 h at 400 °C.

The mixed oxide TiO_2-ZrO_2 with a molar ratio (75–25%) was also prepared using the same method. For that, 0.01 mol of ZrO_2 was dispersed in water and stirred for 24 h at room temperature; then, 0.11 mol of titanium isopropoxide solubilized in propanol was added. The pH was adjusted to 3 and the solution was stirred for 24 h at 60 °C. The sample was dried for 8 h at 80 °C and finally calcined for 2 h at 400 °C.

3.2.3. Catalysts Characterization

Thermogravimetric (TG) analysis of the samples was performed on a LINSEIS.STA.PT 1600 using 8 mg of the catalyst in a flow of air with a Mettler TA 4000 system from 25 to 800 °C at a heating rate of 10 °C·min^{-1}. The textural properties were determined by adsorption/desorption of N_2 at −196 °C using quantachrome Nova 1000 equipment. Before adsorption, the sample was outgassed at 250 °C overnight. The surface area (S_{BET}) was calculated according to the Brunauer–Emmett–Teller (BET) method. The morphology of samples was studied using scanning electron microscopy (SEM) using a LEO (Carl Zeiss) GEMINI-1530 microscope. The crystallinity of samples was determined by powder X-ray diffraction (XRD) on a Rigaku-Miniflex 600 apparatus equipped with a copper anode (λ Kα = 1.5406 Å) and a graphite monochromator. The analyses were carried out at room temperature in the 2θ range between 10° and 80° with a step of 0.04° and an acquisition time of 2 s. The average powder crystallite sizes (D) of the dried materials after heat treatment were estimated using the Scherrer equation with the full width at half maximum (FWHM) of the most intense peak [84,85]:

$$D = k\lambda / (\beta \cdot \cos\theta) \tag{9}$$

where D is the crystal size (nm), k is the Scherrer constant, λ is the monochromatic radiation wavelength (nm), θ is the Bragg angle (rad), and β is the peak width (rad).

Optical absorption spectra were collected on a double-beam UV-Visible spectrophotometer (CARY 5E from VARIAN, Varian (Madrid, Spain)) equipped with a Praying Mantis diffuse reflectance accessory (DRS). The band gap (E_g) of samples was calculated from the reflectance spectra using the Kulbelka–Munk (KM) method. The FTIR spectra of solid samples were recorded using an Agilent Technologies Cary 60 series FTIR spectrometer with ATR accessories in the measurement range of 400–4000 cm^{-1}. X-ray photoelectron spectroscopy (XPS) was carried out using a Kratos Axis Ultra-DLD spectrometer equipped with a hemispherical electron analyzer connected to a DLD (delay-line detector) and an Al-Kα monochromator with a power rating of 600 W. The X-ray source employed was a Mg/Al double anode with a power output of 450 W.

3.2.4. Photocatalytic Tests

Initially, the photoreactor used in this study was equipped with a low-pressure mercury vapor lamp, which operates at near room temperature. The UV lamp is a pen lamp with a diameter of 6.5 mm and a length of 53.8 mm and is protected from the solution by a quartz tube placed in an axial position. The excitation of the mercury atoms allows the emission of radiation by dint of the electric discharge between the electrodes. Monochromatic radiation of 254 nm is emitted by a low-pressure mercury vapor lamp (TNN 15/32, nominal power 15 W). Furthermore, the reaction was carried out using a glass photoreactor placed inside an LEDBOX composed of two blue LEDs (l = 465 nm, 40 W power). In both cases, the antibiotic drug "sulfamethoxazole $C_{10}H_{11}N_3O_3S$" (SMX) was selected as a model pollutant as it is a sulfonamide antibiotic commonly used for treating urinary tract infections, toxoplasmosis, and sinusitis [86]. The degradation kinetics was followed by UV-Vis spectroscopy using a previously calibrated UV-Vis spectrophotometer. Catalytic photodegradation was carried out using 0.1 g of the photocatalyst, previously saturated with the pollutant in the dark to avoid the influence of the different adsorption performances of each sample on the evolution of the SMX concentration. The samples were kept

in contact for 2 days. The concentration was measured at the beginning and end of the day. Since the porosity and volume of mesopores for the adsorption of the samples were low, the adsorption quantity was low and equilibrium was reached after the first day. For example, the initial concentration for the TiO_2 sample was 12 mg/L at the beginning and 11.8 at the end of the first day. At the end of the second day, it was 11.8 mg/L. One day is enough to achieve equilibrium; however, we used a duration of 2 days to ensure saturation. After the 48 h for adsorption equilibrium, the solution concentration was measured by spectrophotometer UV and a few drops of the SMX solution were added until 12 mg/L was reached. Then, the lamps were switched on, and this timepoint was considered the starting degradation time; at regular intervals, an equal sample was taken from the reactor and filtered, and the concentration was measured by UV spectrometry.

The mineralization degrees after each photocatalytic test under blue LED were estimated by measuring the total organic carbon (TOC) using a Shimadzu V-CSH analyzer with an ASI-V autosampler and subtracting the inorganic carbon value in each sample from the total carbon value. Finally, toxicity tests of the solutions of the best photocatalyst were performed using the normalized biotest (UNE/EN/ISO 11345-2 [87]) of luminescent inhibition of Vibrio Fischeribacteria using the LUMIStox 300 system (Dr.LangeGmbH, Hannover, Germany) with a LUMIStherm incubator. Toxicity was quantified as the inhibition (I) percentage after 15 min of exposure in reference to a stock saline solution.

4. Conclusions

In this work, ZrO_2, TiO_2, TiO_2-ZrO_2, and ZrO_2-TiO_2 were successfully synthesized using the simple sol–gel method, characterized, and used in the photocatalytic degradation of Sulfamethoxazole (SMX). SEM, XRD, UV-Vis, N_2 adsorption/desorption, FTIR, ATG, and XPS characterization confirmed the successful formation of mixed oxides. Notably, XRD confirmed the insertion of zirconia into the titania crystal structure when XPS revealed a high presence of oxygen vacancies and defects on the surface of the mixed oxides, particularly the TiO_2-ZrO_2 sample, which improved the textural and structural properties and induced enhanced photocatalytic properties. Among the synthesized materials, TiO_2-ZrO_2 showed the highest degradation efficiency for SMX under both UV and blue LED irradiation with 100% and 76%, respectively. Furthermore, the results of the mineralization degree and toxicity correlated well with the degradation results.

Conflicts of Interest: The authors declare no conflicts of interest.

References

1. Muralikrishna, I.V.; Manickam, V. Industrial wastewater treatment technologies, recycling, and reuse. In *Environmental Management*; Elsevier: Amsterdam, The Netherlands, 2017; pp. 295–336.
2. Oller, I.; Malato, S.; Sánchez-Pérez, J. Combination of advanced oxidation processes and biological treatments for wastewater decontamination—A review. *Sci. Total Environ.* **2011**, *409*, 4141–4166. [CrossRef] [PubMed]
3. Ternes, T.A. Analytical methods for the determination of pharmaceuticals in aqueous environmental samples. *TrAC Trends Anal. Chem.* **2001**, *20*, 419–434. [CrossRef]
4. Kümmerer, K. Introduction: Pharmaceuticals in the environment. In *Pharmaceuticals in the Environment: Sources, Fate, Effects and Risks*; Springer: Berlin/Heidelberg, Germany, 2001; pp. 1–8.
5. Kanakaraju, D.; Glass, B.D.; Oelgemöller, M. Titanium dioxide photocatalysis for pharmaceutical wastewater treatment. *Environ. Chem. Lett.* **2013**, *12*, 27–47. [CrossRef]
6. Kutuzova, A.; Dontsova, T.; Kwapinski, W. Application of TiO_2-Based Photocatalysts to Antibiotics Degradation: Cases of Sulfamethoxazole, Trimethoprim and Ciprofloxacin. *Catalysts* **2021**, *11*, 728. [CrossRef]
7. Wang, J.; Wang, S. Removal of pharmaceuticals and personal care products (PPCPs) from wastewater: A review. *J. Environ. Manag.* **2016**, *182*, 620–640. [CrossRef]
8. Liu, Z.H.; Kanjo, Y.; Mizutani, S. Removal mechanisms for endocrine disrupting compounds (EDCs) in wastewater treatment—Physical means, biodegradation, and chemical advanced oxidation: A review. *Sci. Total Environ.* **2009**, *407*, 731–748. [CrossRef] [PubMed]
9. Mojiri, A.; Zhou, J.; Vakili, M.; Van Le, H. Removal performance and optimisation of pharmaceutical micropollutants from synthetic domestic wastewater by hybrid treatment. *J. Contam. Hydrol.* **2020**, *235*, 103736. [CrossRef]
10. Biń, A.K.; Sobera-Madej, S. Comparison of the Advanced Oxidation Processes (UV, UV/H_2O_2 and O_3) for the Removal of Antibiotic Substances during Wastewater Treatment. *Ozone-Sci. Eng.* **2012**, *34*, 136–139. [CrossRef]
11. Zhang, Q.; Du, R.; Tan, C.; Chen, P.; Yu, G.; Deng, S. Efficient degradation of typical pharmaceuticals in water using a novel TiO_2/ONLH nano-photocatalyst under natural sunlight. *J. Hazard. Mater.* **2021**, *403*, 123582. [CrossRef]
12. Feng, L.; van Hullebusch, E.D.; Rodrigo, M.A.; Esposito, G.; Oturan, M.A. Removal of residual anti-inflammatory and analgesic pharmaceuticals from aqueous systems by electrochemical advanced oxidation processes. A review. *Chem. Eng. J.* **2013**, *228*, 944–964. [CrossRef]
13. Li, C.; Mei, Y.; Qi, G.; Xu, W.; Zhou, Y.; Shen, Y. Degradation characteristics of four major pollutants in chemical pharmaceutical wastewater by Fenton process. *J. Environ. Chem. Eng.* **2021**, *9*, 104564. [CrossRef]
14. Adityosulindro, S.; Barthe, L.; Gonzalez-Labrada, K.; Jauregui Haza, U.J.; Delmas, H.; Julcour, C. Sonolysis and sono-Fenton oxidation for removal of ibuprofen in (waste)water. *Ultrason. Sonochem.* **2017**, *39*, 889–896. [CrossRef] [PubMed]
15. Deng, Y.; Zhao, R. Advanced Oxidation Processes (AOPs) in Wastewater Treatment. *Curr. Pollut. Rep.* **2015**, *1*, 167–176. [CrossRef]
16. Lacombe, S.; Tran-Thi, T.; Guillard, C.; Herrmann, J.; Keller-Spitzer, V.; Keller, N.; Maurette, M.; Pichat, P.; Pigot, T.; Pulgarin, C. La photocatalyse pour l'elimination des polluants. *Actual. Chim.* **2007**, *308*, 79.
17. Agrios, A.G.; Pichat, P. State of the art and perspectives on materials and applications of photocatalysis over TiO_2. *J. Appl. Electrochem.* **2005**, *35*, 655–663. [CrossRef]
18. Vaiano, V.; Sacco, O.; Sannino, D.; Ciambelli, P. Photocatalytic removal of spiramycin from wastewater under visible light with N-doped TiO_2 photocatalysts. *Chem. Eng. J.* **2015**, *261*, 3–8. [CrossRef]
19. Elmolla, E.S.; Chaudhuri, M. The feasibility of using combined TiO_2 photocatalysis-SBR process for antibiotic wastewater treatment. *Desalination* **2011**, *272*, 218–224. [CrossRef]
20. Luttrell, T.; Halpegamage, S.; Tao, J.; Kramer, A.; Sutter, E.; Batzill, M. Why is anatase a better photocatalyst than rutile?-Model studies on epitaxial TiO_2 films. *Sci. Rep.* **2014**, *4*, 4043. [CrossRef]
21. Matos, J.; Montana, R.; Rivero, E.; Escudero, A.; Uzcategui, D. Influence of anatase and rutile phase in TiO_2 upon the photocatalytic degradation of methylene blue under solar irradiation in presence of activated carbon. *Water Sci. Technol.* **2014**, *69*, 2184–2190. [CrossRef]
22. Pelaez, M.; Nolan, N.T.; Pillai, S.C.; Seery, M.K.; Falaras, P.; Kontos, A.G.; Dunlop, P.S.M.; Hamilton, J.W.J.; Byrne, J.A.; O'Shea, K.; et al. A review on the visible light active titanium dioxide photocatalysts for environmental applications. *Appl. Catal. B Environ.* **2012**, *125*, 331–349. [CrossRef]
23. Botta, S.G.; Navio, J.A.; Hidalgo, M.C.; Restrepo, G.M.; Litter, M.I. Photocatalytic properties of ZrO_2 and Fe/ZrO_2 semiconductors prepared by a sol–gel technique. *J. Photochem. Photobiol. A Chem.* **1999**, *129*, 89–99. [CrossRef]
24. Xu, Z.; Yang, Q.; Xie, C.; Yan, W.; Du, Y. Structure, luminescence properties and photocatalytic activity of europium doped-TiO_2 nanoparticles. *J. Mater. Sci.* **2005**, *40*, 1539–1541. [CrossRef]
25. Thabet, S.M.; Abdelhamid, H.N.; Ibrahim, S.A.; El-Bery, H.M. Boosting photocatalytic water splitting of TiO_2 using metal (Ru, Co, or Ni) co-catalysts for hydrogen generation. *Sci. Rep.* **2024**, *14*, 10115. [CrossRef] [PubMed]
26. Li, L.; Chen, X.; Quan, X.; Qiu, F.; Zhang, X. Synthesis of CuO_x/TiO_2 Photocatalysts with Enhanced Photocatalytic Performance. *ACS Omega* **2023**, *8*, 2723–2732. [CrossRef]
27. Karunakaran, C.; Senthilvelan, S. Photocatalysis with ZrO_2: Oxidation of aniline. *J. Mol. Catal. A Chem.* **2005**, *233*, 1–8. [CrossRef]

28. Polisetti, S.; Deshpande, P.A.; Madras, G. Photocatalytic Activity of Combustion Synthesized ZrO$_2$ and ZrO$_2$–TiO$_2$ Mixed Oxides. *Ind. Eng. Chem. Res.* **2011**, *50*, 12915–12924. [CrossRef]

29. Kralik, B.; Chang, E.K.; Louie, S.G. Structural properties and quasiparticle band structure of zirconia. *Phys. Rev. B* **1998**, *57*, 163–1829. [CrossRef]

30. Binitha, N.; Yaakob, Z.; Resmi, R. Influence of synthesis methods on zirconium doped titania photocatalysts. *Open Chem.* **2010**, *8*, 182–187. [CrossRef]

31. Vishwanathan, V.; Roh, H.-S.; Kim, J.-W.; Jun, K.-W. Surface properties and catalytic activity of TiO$_2$–ZrO$_2$ mixed oxides in dehydration of methanol to dimethyl ether. *Catal. Lett.* **2004**, *96*, 23–28. [CrossRef]

32. Bailón-García, E.; Elmouwahidi, A.; Carrasco-Marín, F.; Pérez-Cadenas, A.F.; Maldonado-Hódar, F.J. Development of Carbon-ZrO$_2$ composites with high performance as visible-light photocatalysts. *Appl. Catal. B Environ.* **2017**, *217*, 540–550. [CrossRef]

33. Jiang, B.; Zhang, S.; Guo, X.; Jin, B.; Tian, Y. Preparation and photocatalytic activity of CeO$_2$/TiO$_2$ interface composite film. *Appl. Surf. Sci.* **2009**, *255*, 5975–5978. [CrossRef]

34. Zheng, R.; Meng, X.; Tang, F. Synthesis, characterization and photodegradation study of mixed-phase titania hollow submicrospheres with rough surface. *Appl. Surf. Sci.* **2009**, *255*, 5989–5994. [CrossRef]

35. McManamon, C.; Holmes, J.D.; Morris, M.A. Improved photocatalytic degradation rates of phenol achieved using novel porous ZrO$_2$-doped TiO$_2$ nanoparticulate powders. *J. Hazard. Mater.* **2011**, *193*, 120–127. [CrossRef]

36. Sandoval, S.; Yang, J.; Alfaro, J.G.; Liberman, A.; Makale, M.; Chiang, C.E.; Schuller, I.K.; Kummel, A.C.; Trogler, W.C. Europium Doped TiO$_2$ Hollow Nanoshells: Two-Photon Imaging of Cell Binding. *Chem. Mater.* **2012**, *24*, 4222–4230. [CrossRef] [PubMed]

37. Li, P.; Guo, M.; Qiang, W.; Li, Z.; Wang, C.; Chen, N.; Wang, C.-C.; Wan, C.; Chen, S. Controllable synthesis of cerium zirconium oxide nanocomposites and their application for photocatalytic degradation of sulfonamides. *Appl. Catal. B Environ.* **2019**, *259*, 107–118. [CrossRef]

38. Ding, P.; Ji, H.; Li, P.; Liu, Q.; Wu, Y.; Guo, M.; Zhou, Z.; Gao, S.; Xu, W.; Liu, W.; et al. Visible-light degradation of antibiotics catalyzed by titania/zirconia/graphitic carbon nitride ternary nanocomposites: A combined experimental and theoretical study. *Appl. Catal. B Environ.* **2022**, *300*, 120633. [CrossRef]

39. Aguirre-Cortés, J.M.; Munguía-Ubierna, A.; Moral-Rodríguez, A.; Pérez-Cadenas, A.F.; Carrasco-Marín, F.; Bailón-García, E. Size-miniaturization of TiO$_2$-ZrO$_2$ coupled semiconductors to develop highly efficient visible- driven photocatalysts for the degradation of drugs in wastewater. *Appl. Surf. Sci.* **2024**, *670*, 160609. [CrossRef]

40. Hammami, R.; Aïssa, S.B.; Batis, H. Effects of thermal treatment on physico-chemical and catalytic properties of lanthanum manganite LaMnO$_{3+y}$. *Appl. Catal. A Gen.* **2009**, *353*, 145–153. [CrossRef]

41. Kite, S.V.; Sathe, D.J.; Kadam, A.N.; Chavan, S.S.; Garadkar, K.M. Highly efcient photodegradation of 4-nitrophenol over the nano-TiO$_2$ obtained from chemical bath deposition technique. *Res. Chem. Intermed.* **2020**, *46*, 1255–1282. [CrossRef]

42. Prime, R.B.; Bair, H.E.; Vyazovkin, S.; Gallagher, P.K.; Riga, A. 3. Thermogravimetric analysis (TGA). In *Thermal Analysis of Polymers. Fundamentals and Applications*; Wiley: Hoboken, NJ, USA, 2009; pp. 241–314.

43. Vahid, B.R.; Haghighi, M. Biodiesel production from sunflower oil over MgO/MgAl$_2$O$_4$ nanocatalyst: Effect of fuel type on catalyst nanostructure and performance. *Energy Convers. Manag.* **2017**, *134*, 290–300. [CrossRef]

44. Kambur, A.; Pozan, G.S.; Boz, I. Preparation, characterization and photocatalytic activity of TiO$_2$–ZrO$_2$ binary oxide nanoparticles. *Appl. Catal. B Environ.* **2012**, *115*–*116*, 149–158. [CrossRef]

45. Zare, M.H.; Mehrabani-Zeinabad, A. Photocatalytic activity of ZrO$_2$/TiO$_2$/Fe$_3$O$_4$ ternary nanocomposite for the degradation of naproxen: Characterization and optimization using response surface methodology. *Sci. Rep.* **2022**, *12*, 10388. [CrossRef] [PubMed]

46. Ökte, A.N.; Sayınsöz, E. Characterization and photocatalytic activity of TiO$_2$ supported sepiolite catalysts. *Sep. Purif. Technol.* **2008**, *62*, 535–543. [CrossRef]

47. Chen, K.; Li, J.; Wang, W.; Zhang, Y.; Wang, X.; Su, H. The preparation of vanadium-doped TiO$_2$–montmorillonite nanocomposites and the photodegradation of sulforhodamine B under visible light irradiation. *Appl. Surf. Sci.* **2011**, *257*, 7276–7285. [CrossRef]

48. Wu, C.; Zhao, X.; Ren, Y.; Yue, Y.; Hua, W.; Cao, Y.; Tang, Y.; Gao, Z. Gas-phase photo-oxidations of organic compounds over different forms of zirconia. *J. Mol. Catal. A Chem.* **2005**, *229*, 233–239. [CrossRef]

49. Basahel, S.N.; Ali, T.T.; Mokhtar, M.; Narasimharao, K. Influence of crystal structure of nanosized ZrO$_2$ on photocatalytic degradation of methyl orange. *Nanoscale Res. Lett.* **2015**, *10*, 73. [CrossRef]

50. Behbahani, A.; Rowshanzamir, S.; Esmaeilifar, A. Hydrothermal Synthesis of Zirconia Nanoparticles from Commercial Zirconia. *Procedia Eng.* **2012**, *42*, 908–917. [CrossRef]

51. Jayakumar, S.; Ananthapadmanabhan, P.V.; Thiyagarajan, T.K.; Perumal, K.; Mishra, S.C.; Suresh, G.; Su, L.T.; Tok, A.I.Y. Nanosize stabilization of cubic and tetragonal phases in reactive plasma synthesized zirconia powders. *Mater. Chem. Phys.* **2013**, *140*, 176–182. [CrossRef]

52. George, A.; Solomon, S.; Thomas, J.K.; John, A. Characterizations and electrical properties of ZrTiO$_4$ ceramic. *Mater. Res. Bull.* **2012**, *47*, 3141–3147. [CrossRef]

53. Srinivasan, R.; De Angelis, R.J.; Ice, G.; Davis, B.H. Identification of tetragonal and cubic structures of zirconia using synchrotron x-radiation source. *Mater. Res. Soc.* **1991**, *6*, 1287–1292. [CrossRef]

54. Kumari, L.; Li, W.; Wang, D. Monoclinic zirconium oxide nanostructures synthesized by a hydrothermal route. *Nanotechnology* **2008**, *19*, 195602. [CrossRef] [PubMed]

55. Liu, F.; Yan, X.; Chen, X.; Tian, L.; Xia, Q.; Chen, X. Mesoporous TiO_2 nanoparticles terminated with carbonate-like groups: Amorphous/crystalline structure and visible-light photocatalytic activity. *Catal. Today* **2016**, *264*, 243–249. [CrossRef]

56. Wang, S.; Fang, Y.; Huang, Z.; Xu, H.; Shen, W. The Effects of the Crystalline Phase of Zirconia on C–O Activation and C–C Coupling in Converting Syngas into Aromatics. *Catalysts* **2020**, *10*, 262. [CrossRef]

57. Das, I.; Chattopadhyay, S.; Mahato, A.; Kundu, B.; De, G. Fabrication of a cubic zirconia nanocoating on a titanium dental implant with excellent adhesion, hardness and biocompatibility. *RSC Adv.* **2016**, *6*, 59030–59038. [CrossRef]

58. Kelly, A.; Knowles, K.M. Appendix 7: Crystal Structure Data. In *Crystallography and Crystal Defects*; Wiley: Hoboken, NJ, USA, 2012; pp. 491–498.

59. Toraya, H.; Yoshimura, M.; Somiya, S. Calibration curve for quantitative analysis of the monoclinic-tetragonal ZrO_2 system by X-ray diffraction. *J. Am. Ceram. Soc.* **1984**, *67*, 119–121. [CrossRef]

60. Heshmatpour, F.; Aghakhanpour, R.B. Synthesis and characterization of nanocrystalline zirconia powder by simple sol–gel method with glucose and fructose as organic additives. *Powder Technol.* **2011**, *205*, 193–200. [CrossRef]

61. Tahmasebpour, M.; Babaluo, A.A.; Aghjeh, M.K.R. Synthesis of zirconia nanopowders from various zirconium salts via polyacrylamide gel method. *J. Eur. Ceram. Soc.* **2008**, *28*, 773–778. [CrossRef]

62. Bhaskar, S.; Awin, E.W.; Kumar, K.H.; Lale, A.; Bernard, S.; Kumar, R. Design of nanoscaled heterojunctions in precursor-derived t-ZrO_2/SiOC (N) nanocomposites: Transgressing the boundaries of catalytic activity from UV to visible light. *Sci. Rep.* **2020**, *10*, 430. [CrossRef]

63. Khattab, E.-S.R.; Abd El Rehim, S.S.; Hassan, W.M.; El-Shazly, T.S. Band structure engineering and optical properties of pristine and doped monoclinic zirconia (m-ZrO_2): Density functional theory theoretical prospective. *ACS Omega* **2021**, *6*, 30061–30068. [CrossRef]

64. Honda, M.; Ochiai, T.; Listiani, P.; Yamaguchi, Y.; Ichikawa, Y. Low-Temperature Synthesis of Cu-Doped Anatase TiO_2 Nanostructures via Liquid Phase Deposition Method for Enhanced Photocatalysis. *Materials* **2023**, *16*, 639. [CrossRef]

65. Chang, S.-M.; Doong, R.-A. Interband Transitions in Sol-Gel-Derived ZrO_2 Films under Different Calcination Conditions. *Chem. Mater.* **2007**, *19*, 4804–4810. [CrossRef]

66. Katsumata, H.; Makita, Y.; Kobayashi, N.; Shibata, H.; Hasegawa, M.; Aksenov, I.; Kimura, S.; Obara, A.; Uekusa, S.-I. Optical absorption and photoluminescence studies of β-$FeSi_2$ prepared by heavy implantation of Fe^+ ions into Si. *J. Appl. Phys.* **1996**, *80*, 5955–5962. [CrossRef]

67. Hidalgo, N.; Colon, G.; Botta, S.; Litter, M. Preparation and physicochemical properties of ZrO_2 and Fe/ZrO_2 prepared by a sol–gel technique. *Langmuir* **2001**, *17*, 202–210.

68. Simon, S.M.; George, G.; Chandran, A.; Prakashan, V.P.; Sajna, M.S.; Saritha, A.C.; Biju, P.R.; Joseph, C.; Unnikrishnan, N.V. Morphological and thermal studies of mesoporous TiO_2-ZrO_2 and TiO_2-ZrO_2-polymer composites as potential self cleaning surface. *Mater. Today Proc.* **2020**, *33*, 1327–1332. [CrossRef]

69. Gao, N.; Zhou, Y.; Fan, M.; Xu, H.; Chen, Y.; Shen, S. Promoting effect and role of alkaline earth metal added to ZrO_2-TiO_2-supported CeO_2 for dichloromethane oxidation. *Chem. Eng. J.* **2020**, *396*, 125193. [CrossRef]

70. Fang, D.; Luo, Z.; Liu, S.; Zeng, T.; Liu, L.; Xu, J.; Bai, Z.; Xu, W. Photoluminescence properties and photocatalytic activities of zirconia nanotube arrays fabricated by anodization. *Opt. Mater.* **2013**, *35*, 1461–1466. [CrossRef]

71. Saleem, A.M.; Gnanasaravanan, S.; Saravanakkumar, D.; Rajasekar, S.; Ayeshamariam, A.; Jayachandran, M. Preparation and characterization studies of TiO_2 doped ZrO_2 on ITO nanocomposites for optoelectronic applications. *Mater. Today Proc.* **2021**, *36*, 408–415. [CrossRef]

72. Pipornpong, W.; Wanbayor, R.; Ruangpornvisuti, V. Adsorption CO_2 on the perfect and oxygen vacancy defect surfaces of anatase TiO_2 and its photocatalytic mechanism of conversion to CO. *Appl. Surf. Sci.* **2011**, *257*, 10322–10328. [CrossRef]

73. Indrakanti, V.P.; Kubicki, J.D.; Schobert, H.H. Photoinduced activation of CO_2 on TiO_2 surfaces: Quantum chemical modeling of CO_2 adsorption on oxygen vacancies. *Fuel Process. Technol.* **2011**, *92*, 805–811. [CrossRef]

74. Adam, F.; Chew, T.-S.; Andas, J. Liquid Phase Oxidation of Acetophenone over Rice Husk Silica Vanadium Catalyst. *Chin. J. Catal.* **2012**, *33*, 518–522. [CrossRef]

75. Bailón-García, E.; Elmouwahidi, A.; Álvarez, M.A.; Carrasco-Marín, F.; Pérez-Cadenas, A.F.; Maldonado-Hódar, F.J. New carbon xerogel-TiO_2 composites with high performance as visible-light photocatalysts for dye mineralization. *Appl. Catal. B Environ.* **2017**, *201*, 29–40. [CrossRef]

76. Gao, L.S.; Zhang, S.N.; Zou, X.; Wang, J.; Su, J.; Chen, J.S. Oxygen Vacancy Engineering of Titania-Induced by Sr^{2+} Dopants for Visible-Light-Driven Hydrogen Evolution. *Inorg. Chem.* **2021**, *60*, 32–36. [CrossRef]

77. Hamad, H.; Bailón-García, E.; Pérez-Cadenas, A.F.; Maldonado-Hódar, F.J.; Carrasco-Marín, F. ZrO_2-TiO_2/Carbon core-shell composites as highly efficient solar-driven photo-catalysts: An approach for removal of hazardous water pollutants. *J. Environ. Chem. Eng.* **2020**, *8*, 104350. [CrossRef]

78. Reddy, C.V.; Babu, B.; Reddy, I.N.; Shim, J. Synthesis and characterization of pure tetragonal ZrO_2 nanoparticles with enhanced photocatalytic activity. *Ceram. Int.* **2018**, *44*, 6940–6948. [CrossRef]

79. Mishra, S.; Debnath, A.K.; Muthe, K.P.; Das, N.; Parhi, P. Rapid synthesis of tetragonal zirconia nanoparticles by microwave-solvothermal route and its photocatalytic activity towards organic dyes and hexavalent chromium in single and binary component systems. *Colloids Surf. A Physicochem. Eng. Asp.* **2021**, *608*, 125551. [CrossRef]

80. Ahmed, O.; Pons, M.-N.; Lachheb, H.; Houas, A.; Zahraa, O. Degradation of sulfamethoxazole by photocatalysis using supported TiO$_2$. *Sustain. Environ. Res.* **2014**, *24*, 381–387.

81. Kim, J.R.; Kan, E. Heterogeneous Photocatalytic Degradation of Sulfamethoxazole in Water Using a Biochar-Supported TiO$_2$ Photocatalyst. *J. Environ. Manag.* **2016**, *180*, 94–101. [CrossRef]

82. Hamad, H.; Bailón-García, E.; Maldonado-Hódar, F.J.; Pérez-Cadenas, A.F.; Carrasco-Marín, F.; Morales-Torres, S. Synthesis of Ti$_x$O$_y$ nanocrystals in mild synthesis conditions for the degradation of pollutants under solar light. *Appl. Catal. B Environ.* **2019**, *241*, 385–392. [CrossRef]

83. Jahdi, M.; Mishra, S.B.; Nxumalo, E.N.; Mhlanga, S.D.; Mishra, A.K. Smart pathways for the photocatalytic degradation of sulfamethoxazole drug using F-Pd co-doped TiO$_2$ nanocomposites. *Appl. Catal. B Environ.* **2020**, *267*, 118716. [CrossRef]

84. Monshi, A.; Foroughi, M.R.; Monshi, M.R. Modified Scherrer Equation to Estimate More Accurately Nano-Crystallite Size Using XRD. *World J. Nano Sci. Eng.* **2012**, *2*, 154–160. [CrossRef]

85. Szepesi, C.J.; Adair, J.H.; Chan, H. High Yield Hydrothermal Synthesis of Nano-Scale Zirconia and YTZP. *J. Am. Ceram. Soc.* **2011**, *94*, 4239–4246. [CrossRef]

86. Balarak, D.; Mostafapour, F.K. Batch equilibrium, kinetics and thermodynamics study of sulfamethoxazole antibiotics onto Azolla filiculoides as a novel biosorbent. *Br. J. Pharm. Res.* **2016**, *13*, 1–14. [CrossRef]

87. *ISO 11348-2:2007/Amd 1:2018*; Water Quality—Determination of the Inhibitory Effect of Water Samples on the Light Emission of Vibrio Fischeri (Luminescent Bacteria Test)—Part 2: Method Using Liquid-Dried Bacteria—Amendment 1. ISO: Geneva, Switzerland, 2018. Available online: https://www.une.org/encuentra-tu-norma/busca-tu-norma/norma?c=N0062815 (accessed on 31 October 2024).